

Anomalous spin projection noise in a spin-exchange-relaxation-free alkali-metal vapor

K. Mouloudakis,^{1,*} J. Kong,^{2,*} A. Sierant,¹ E. Arkin,² M. Hernández Ruiz,¹ R. Jiménez-Martínez,³ and M. W. Mitchell^{1,4}

¹*ICFO - Institut de Ciències Fotòniques, The Barcelona Institute of Science and Technology, 08860 Castelldefels (Barcelona), Spain*

²*Department of Physics, Hangzhou Dianzi University, Hangzhou 310018, China*

³*FieldLine Industries, Boulder, Colorado 80303, USA*

⁴*ICREA - Institució Catalana de Recerca i Estudis Avançats, 08010 Barcelona, Spain*

(Dated: August 1, 2023)

We perform spin-noise spectroscopy on an unpolarized ^{87}Rb vapor in the spin-exchange-relaxation-free (SERF) regime. We observe noise spectral distributions that deviate strongly from Lorentzian models that accurately describe lower-density regimes. For example, at magnetic fields of $\sim 1\ \mu\text{T}$ and ^{87}Rb densities $\gtrsim 1 \times 10^{14}\ \text{atoms}/\text{cm}^3$ we observe an asymmetric spin-noise distribution in which the resonance line is depleted by about half its power, with the diverted power becoming a broad spectral component that could be mistaken for optical shot noise. The results are in good agreement with recent models accounting for correlations between the ground hyperfine states. We discuss implications for quantum sensing and absolute noise calibration in spin-squeezing and entanglement detection.

Quantum noise ultimately limits the performance of atomic sensors including optical clocks [1, 2], magnetometers [3–5], inertial sensors [6], and instruments for fundamental physics [7, 8]. In these sensors atomic quantum noise, or *spin projection noise* (SPN), is rooted in the discreteness of the atom and the quantization of atomic observables, and is shaped by dynamical processes [9, 10]. Such noise can be accurately described using the quantum structure of spin states, spin dynamics [11–13], and the regression theorem [14]. In non- or weakly-interacting atomic media this leads to, for example, Lorentzian-shaped noise-spectral features, characteristic of harmonic oscillators under linear dissipation, as well as spin-noise powers scaling as the number of atoms. These characteristics are employed in absolute calibrations based on the atomic spin structure [15, 16].

An important class of atomic sensors operate outside this weakly-coupled regime, with relaxation dynamics significantly different than in weakly-interacting systems. Of particular interest are magnetometers operated in the spin-exchange-relaxation-free (SERF) regime [17], employed in biomagnetism detection [18], inertial sensors [19], and tests of fundamental physics [20]. In SERF, which occurs in dense alkali vapors, spin-exchange (SE) collisions and hyperfine interactions dominate the spin dynamics, leading to line narrowing of the magnetic resonances and a corresponding boost to the sensitivity [21, 22]. The line shifts and line narrowing associated with the SERF regime are well known from optically-detected magnetic resonance experiments using spin-polarized ensembles [23, 24].

The implications of the SERF physics for spin projection noise are less well explored. An experimental study found that SERF media support and preserve non-classical spin correlations, i.e., entanglement and spin squeezing [25]. In addition, a theoretical study showed

that the spin-exchange interaction can sustain spin correlations for experimentally meaningful timescales [26]. It has recently been predicted [10] that SPN will show importantly non-Lorentzian spectra in the SERF regime with implications for sensing and calibration applications. Here we experimentally study the behavior of SPN of an unpolarized ^{87}Rb ensemble in the SERF regime. Using spin-noise spectroscopy (SNS), i.e., optical detection of thermally-driven ensembles [27–38], we observe the spontaneous spin fluctuations of the vapor across the phase transition to the SERF regime. Unpolarized ensembles are insensitive to magnetic noise, therefore naturally offering a testbed for studying spin fluctuations under minimal interference from technical noise. Our characterization of SPN not only validates the recent predictions [10], but also experimentally demonstrates anomalous spin-noise behavior, including spin-noise redistribution that can affect both the fundamental sensitivity of SERF instruments and the use of spin-noise as a calibrated noise source.

The experimental setup is shown in Fig. 1a. Isotopically enriched ^{87}Rb and 0.12 amg of N_2 buffer gas are held in a cylindrical cell of 12.7 mm diameter and 30 mm internal length, with anti-reflection coated windows of 5 mm thickness. The cell is placed at the center of a cylindrical, four-layer, mu-metal magnetic shield and solenoid and shim coils are used to produce a homogeneous DC magnetic field $\mathbf{B} = (B, 0, 0)$ along the $\hat{\mathbf{x}}$ direction. A ceramic oven, intermittent Joule heating, and a thermocouple are used to control the cell temperature. An external cavity diode laser produces a linearly polarized 795 nm beam detuned 46 GHz to the blue of the D_1 line of ^{87}Rb , monitored with a wavelength meter. The laser output, propagating along $\hat{\mathbf{z}}$, is spatially filtered with a single-mode fiber to produce a Gaussian beam with effective area $A_{\text{eff}} \approx 1.5\ \text{mm}^2$, defined as

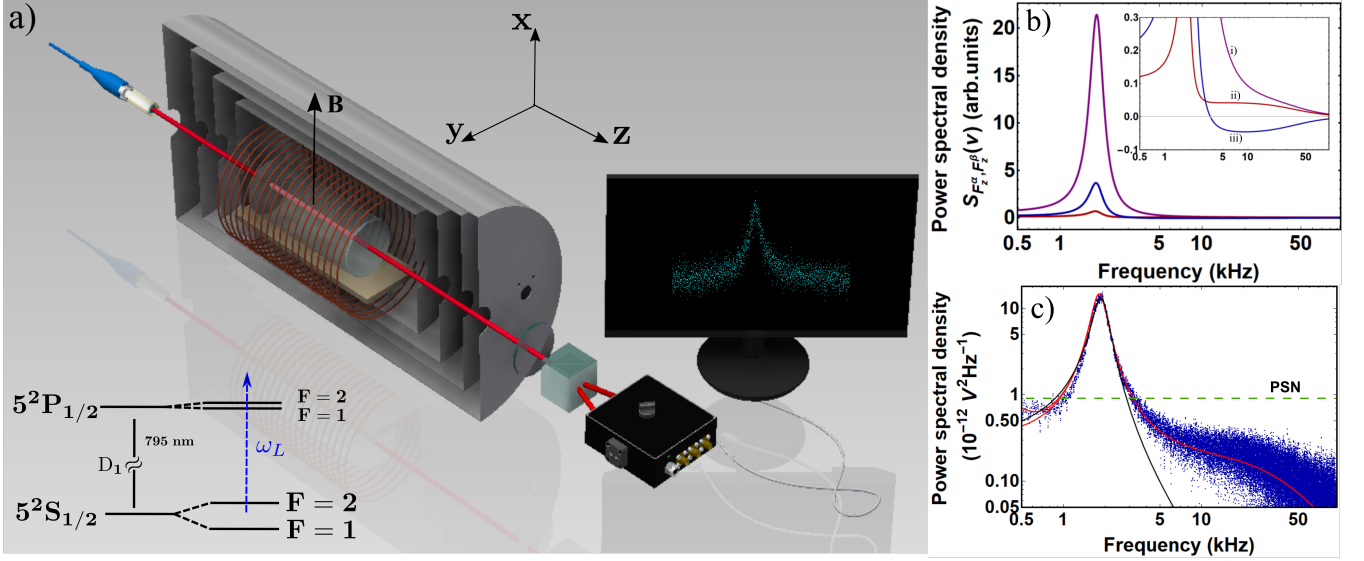


FIG. 1. **a)** Schematic representation of the experimental setup (see text). **b)** Predicted non-Lorentzian spin-noise contributions i) $S_{\hat{F}_z^a, \hat{F}_z^a}(\nu)$, ii) $S_{\hat{F}_z^b, \hat{F}_z^b}(\nu)$, iii) $S_{\hat{F}_z^a, \hat{F}_z^b}(\nu)$ and $S_{\hat{F}_z^b, \hat{F}_z^a}(\nu)$, computed using Eq.(6) and experimentally relevant parameters: $R_{\text{se}} \approx 3.02 \times 10^5 \text{ s}^{-1}$ and $R_{\text{sd}} \approx 0.03 \times 10^5 \text{ s}^{-1}$, corresponding to $3.4 \times 10^{14} \text{ atoms/cm}^3$ and temperature $T = 169^\circ \text{C}$. The magnetic field is $B = 385 \text{ nT}$ along the \hat{x} direction. **c)** Spin-noise spectra acquired at a magnetic field of $B = 385 \text{ nT}$ and a number density of $n \approx 3.4 \times 10^{14} \text{ atoms/cm}^3$. The mean PSN level is depicted by the green dashed line and has been subtracted from the spectrum. Data are fitted by a Lorentzian model (black solid line) and red lines and Eq.(1) (red solid lines) with and without “1/f-noise”. The departure from the Lorentzian spectrum is demonstrated.

$A_{\text{eff}} = L[\int I(x, y, z) dx dy]^2 / \int I^2(x, y, z) dx dy dz$, where $I(x, y, z)$ is the intensity of the Gaussian beam and L the length of the cell. The intensity is measured with a beam profiler. The effective number of atoms probed by the laser beam is $N_{\text{at}} = n A_{\text{eff}} L$, where n is the alkali number density. Both the detuning of the light and the atomic 2.4 GHz full-width at half maximum (FWHM) pressure-broadened optical linewidth are larger than the 0.8 GHz hyperfine splitting of the excited state, so tensor polarizability effects are expected to be negligible [39]. The transmitted light is detected by a balanced polarimeter comprised of a half-waveplate, a Wollaston prism and an amplified differential photodetector (PD). The PD signal is recorded by a 24 bit digitizer for later processing.

The experimentally obtained noise-spectra are of the form

$$S_{\text{opt}}(\nu) = S_{\text{psn}} + S_{1/f}(\nu) + S_{\text{el}}(\nu) + S_{\text{at}}(\nu), \quad (1)$$

where the contribution from photon shot noise (PSN) is $S_{\text{psn}} = 2G^2 q_e r P \approx 0.91 \times 10^{-12} \text{ V}^2 \text{ Hz}^{-1}$, with $q_e \approx 1.9 \times 10^{-19} \text{ C}$ being the electron charge, $r \approx 0.52 \text{ A W}^{-1}$ at 795 nm the PD responsivity, $G = 1 \times 10^5 \text{ V A}^{-1}$ the transimpedance gain of the PD and $P \approx 550 \text{ }\mu\text{W}$ the laser power reaching the polarimeter. $S_{1/f} = \zeta^2 \nu^{-\beta}$, $\beta > 0$ is “1/f noise” with strength ζ^2 , and $S_{\text{el}}(\nu)$ is the electronic noise of the PD and acquisition system, which in practice is about 20 dB below the PSN background. The last term in Eq.(1) is the atomic spin noise spectrum, presenting a resonance feature at the spin pre-

cession frequency. The spin-noise power of the thermal state is a readily available noise reference, and has been used in noise calibration for spin squeezing [40] and entanglement detection [25] experiments. We note that for frequencies above 0.5 kHz, $S_{1/f}(\nu)$ is negligible, thus, in the analysis that follows $S_{\text{opt}}(\nu)$ is approximated as $S_{\text{opt}}(\nu) \approx S_{\text{at}}(\nu) + S_{\text{psn}}$.

To model the atomic spectra we employ the Ornstein-Uhlenbeck approach as derived in [10] and further discussed in [41]. In this model, the spectra result from the stochastic dynamics of the hyperfine collective spin vectors $\hat{\mathbf{F}}^a(t)$, $\alpha \in \{a = I + 1/2, b = I - 1/2\}$, governed by

$$d\hat{\mathbf{X}}(t) = A\hat{\mathbf{X}}(t)dt + Qd\hat{\mathbf{W}}(t), \quad (2)$$

where $\hat{\mathbf{X}} \equiv [\hat{F}_x^a, \hat{F}_y^a, \hat{F}_z^a, \hat{F}_x^b, \hat{F}_y^b, \hat{F}_z^b]^T$, A is the drift matrix, Q is the noise strength matrix, and $d\hat{\mathbf{W}}$ is a length-six vector of independent Wiener increments [41]. For such processes, with real A and Q , the power spectral density matrix is [14]

$$S_{\hat{\mathbf{X}}, \hat{\mathbf{X}}}(\omega) = -\frac{1}{2\pi} (A + i\omega \mathbb{1})^{-1} Q Q^T (A^T - i\omega \mathbb{1})^{-1}, \quad (3)$$

where $\mathbb{1}$ is the 6×6 identity matrix. In equilibrium, $Q Q^T$ is directly related to A and to the steady-state, equal-time covariance matrix $\mathcal{R}_{\hat{\mathbf{X}}, \hat{\mathbf{X}}}(0)$ by

$$Q Q^T = A \mathcal{R}_{\hat{\mathbf{X}}, \hat{\mathbf{X}}}(0) + \mathcal{R}_{\hat{\mathbf{X}}, \hat{\mathbf{X}}}(0) A^T, \quad (4)$$

where

$$\mathcal{R}_{\hat{F}_i^\alpha, \hat{F}_j^\beta}(0) = \delta_{ij} \delta_{\alpha\beta} \frac{f^\alpha(f^\alpha + 1)(2f^\alpha + 1)}{6(2I + 1)} N_{\text{at}}, \quad (5)$$

where N_{at} is the number of atoms contributing to the spectrum and f^α is the single-atom hyperfine spin value [10]. In this way, it is possible to compute fluctuation spectra for the distinct hyperfine (α) components. A Faraday rotation signal from such a medium has power spectral density [41]

$$S_{\text{at}}(\nu) = \mathcal{A} r^2 G^2 P^2 \left[g_a^2 S_{\hat{F}_z^a, \hat{F}_z^a}(\nu) + g_b^2 S_{\hat{F}_z^b, \hat{F}_z^b}(\nu) - g_a g_b \left(S_{\hat{F}_z^a, \hat{F}_z^b}(\nu) + S_{\hat{F}_z^b, \hat{F}_z^a}(\nu) \right) \right], \quad (6)$$

where \mathcal{A} is a unitless scale factor and g_α is a detuning-dependent coupling proportional to the vector polarizability for the hyperfine state α .

Cross-correlations between the two ground-state hyperfine levels allows for the $g_a g_b$ term in Eq.(6) to partially cancel the g_a^2 and g_b^2 terms, thereby distorting the spectra and affecting the distribution of spin-noise power. The non-Lorentzian character of these spectra is illustrated in Fig. 1b) and 1c). It is these peculiar effects of SPN in the SERF regime that we study below.

Representative spin-noise spectra, acquired as a function of transverse bias field, are shown in Fig. 2. The observed growth and narrowing of the spin-noise resonance with decreasing field are hallmarks of the SERF regime, revealing information about the way spin interactions affect the auto-correlation functions of the system in thermal equilibrium.

We fit the observed spectra with $S_{\text{opt}}(\nu) = S_{\text{at}}(\nu) + S_{\text{psn}}$, with $S_{\text{at}}(\nu)$ from Eq.(6) and photon shot noise $S_{\text{psn}} = 0.91 \times 10^{-12} \text{ V}^2 \text{ Hz}^{-1}$ from an independent measurement. The magnetic field is inferred from the current in the B_x coil, previously calibrated by spin-noise spectroscopy at low density [41]. A simultaneous fit to all spectra finds best-fit parameters $R_{\text{se}} = 3.02 \times 10^5 \text{ s}^{-1}$, $R_{\text{sd}} = 0.03 \times 10^5 \text{ s}^{-1}$, $R = 400 \text{ s}^{-1}$, and $\mathcal{A} = 2.3 \times 10^3$. These are respectively the rates of spin-exchange, spin-destruction and spin-depolarizing processes as defined in [41]. The fitted spectra are shown as black lines in Fig. 2, and agree well except at the lowest field strengths. Deviations from Eq.(6) at low field are expected due to imperfect compensation of remanent fields, the $S_{1/f}(\nu)$ contribution, and diffusion. A complete model accounting both for spin-exchange and atomic diffusion effects is still missing from the literature, however diffusion alone has been extensively studied in [34, 42]. From the fitted value of the spin-exchange rate, the 169°C temperature of the vapor and the $1.9 \times 10^{-14} \text{ cm}^2$ SE cross-section [43], we infer an alkali number density of $3.4 \times 10^{14} \text{ atoms/cm}^3$.

To visualize the “slowing-down” of the spin precession and the linewidth reduction, in Fig. 2 (inset) we compare the observed resonance frequency and linewidth

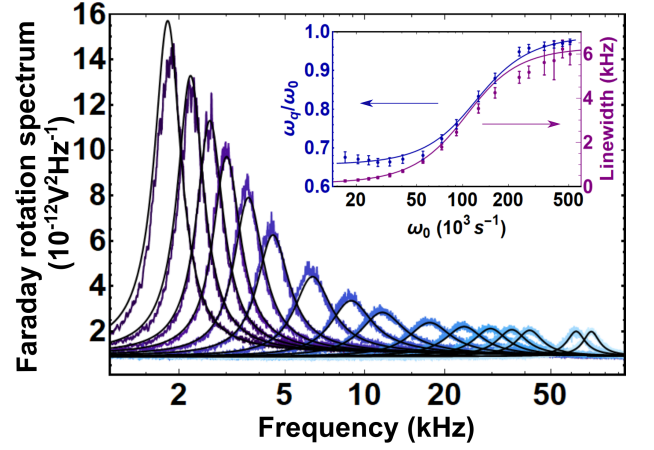


FIG. 2. Single-sided power spectral density (PSD) of the polarimeter signal for transverse magnetic fields ranging from 280 nT to 12 μT while the vapor cell is maintained at approximately 169°C. Each spectrum shows the linear average [41] of 150 spectra, each computed on a 0.5 s acquisition with a sampling rate of 200 kSa s^{-1} . A 20 Hz (ten-bin) boxcar smoothing has also been applied [37]. Black solid lines: fit of Eq.(1) (excluding 1/f and electronic noise) to the observed spectra (see text). Inset: Left axis shows spin-noise precession frequency ω_q normalized to $\omega_0 = g_s \mu_B B / [\hbar(2I + 1)]$, versus ω_0 known by calibration of the coils at low density [41]. Right axis shows the spin-noise linewidth (HWHM) versus ω_0 . Data are obtained by fitting the spectra with a distorted Lorentzian (see text). Error bars show \pm one standard deviation in the fit estimation-parameters over 150 acquisitions. Blue (purple) solid line shows $\text{Im}[\lambda]$ ($\text{Re}[\lambda]$) of the eigenvalues of the drift matrix A , as given by Eq.7 of [41]. The parameters are discussed in the main text.

from distorted-Lorentzian fits to individual spectra [41] against the predictions of Eq. (6) with the above fit parameters. As described in [41], the predicted values can be computed from the real and imaginary parts of the eigenvalues of the drift matrix A . This extends the results of [24] to account for spin-destruction and spin depolarizing processes, for any alkali species.

We now study the redistribution of spin-noise power across the transition from the SE-dominated to the SERF regime. The total atomic noise power in this state is given by

$$\int_0^\infty S_{\text{at}}(\nu) d\nu = \frac{1}{2} \mathcal{A} r^2 G^2 P^2 [g_a^2 \text{var}(F^a) + g_b^2 \text{var}(F^b)], \quad (7)$$

where $\text{var}(F^\alpha)$, $\alpha \in [a, b]$ are given by Eq.(5). Since our acquisition is limited by a 100 kHz Nyquist frequency, the experimentally obtained noise is only a portion of Eq.(7), as discussed in [41]. We stress that the noise in Eq.(7) is independent of the magnetic-resonance parameters and depends only on the number of probed atoms, the probe intensity and detuning, and the optical linewidth.

In the SERF regime, the predicted spectra are non-

Lorentzian, with a significant portion of spin noise spread over the high-frequency part of the spectrum. To demonstrate this, we acquire spectra under a fixed transverse field of $B = 918$ nT and alkali number density across the transition from slow SE ($R_{se} \ll \omega_0$) to rapid SE ($R_{se} \gg \omega_0$), see Fig. 3, inset. We numerically integrate the observed spectra to compute

$$\int_{\nu_{low}}^{\nu_{br}} S_{at}(\nu) d\nu \bigg/ \int_{\nu_{low}}^{\nu_{bw}} S_{at}(\nu) d\nu, \quad (8)$$

which describes the fraction of the observed power below a cut-off frequency ν_{br} . We choose $\nu_{bw} = 95$ kHz as the upper and $\nu_{low} = 0.5$ kHz as the lower limits of integration in order to avoid distortions in the noise power due to the digitizer's anti-aliasing filter and the $1/f$ noise, respectively. The cut-off frequency $\nu_{br} = 20$ kHz is chosen to be a few FWHM above resonance so that, were the line Lorentzian, nearly all the spin noise would be below cut-off. It is seen in Fig. 3 that at low densities nearly all of the atomic noise is below ν_{br} , whereas at higher densities, in the SERF regime, nearly 50% of the noise shifts above ν_{br} . The analogous calculation for different values of ν_{br} is given in [41]. These observations support the picture [10] that $\hat{\mathbf{F}}^a - \hat{\mathbf{F}}^b$ cross-correlations, a consequence of the strong inter-hyperfine coupling in SERF, are important in this regime. The noise distribution of the different hyperfine levels are discussed in [41].

This line reshaping, if not accounted for, can produce systematic errors in calibration based on the atomic noise spectra. For example, an accurate spectral model outside the SERF regime describes a white shot-noise background plus a Lorentzian or sum of Lorentzians representing $S_{at}(\nu)$. The area of the Lorentzians indicates the atomic number, and the shot noise level the optical power. Fitting this model to SERF regime noise spectra would produce an underestimate of the atom number and an over-estimate of the optical power, due to shifting of spin noise power into the long, high-frequency tail of $S_{at}(\nu)$.

Spin-noise redistribution out of the peak at ω_q , while derived and observed here at zero mean polarization, can be expected to occur also in polarized ensembles, at least ones with weak polarization [35]. A variety of magnetometry strategies obtain signals due to spin precession at ω_q , and would thus would have improved signal-to-noise ratio in the SERF regime relative to the SE-dominated regime. This fundamental sensitivity advantage is in addition to the well-known coherence-time advantage in the SERF regime [17, 21, 22].

In conclusion, we have measured and characterized the spin noise of a thermal ^{87}Rb in the transition from the SE-dominated to SERF regimes. We observe anomalous noise lineshapes arising from strong coupling of the ground hyperfine spins in the SERF regime. The line reshaping notably reduces the power in the resonant peak,

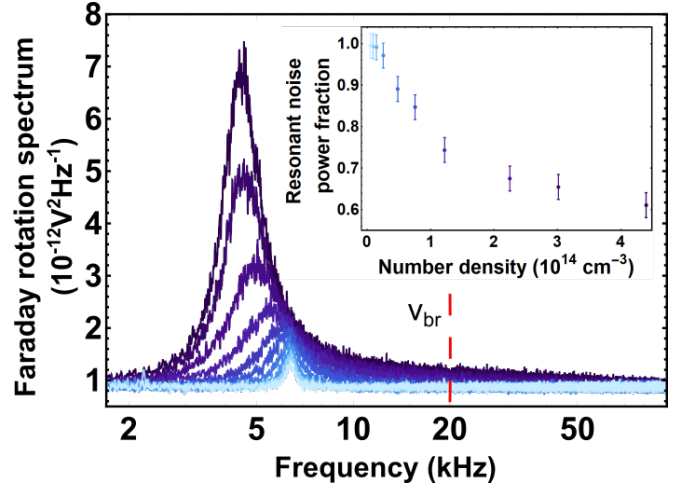


FIG. 3. Spin-noise spectrum (single-sided PSD) as a function of the ^{87}Rb number density for a fixed magnetic field of $B = 918$ nT. Each spectrum shows the linear average of 100 spectra. Long high-frequency tails are apparent. Inset: Resonant noise power fraction as a function of number density as calculated using Eq.(8). The cut-off frequency ν_{br} at 20 kHz is indicated by the red dashed line. Error bars show \pm one standard deviation in the numerical integration over 100 acquisitions.

and produces a broadband component that imitates photon shot noise. The results validate recent theoretical models, improve the accuracy of thermal-state-based noise calibration for spin squeezing and entanglement generation, and suggest a hyperfine-correlation-induced reduction in fundamental quantum noise for optically-pumped magnetometers operating in the SERF regime.

We thank G. Vasilakis, J. Kolodyński and V.G. Lucivero for useful discussions. JK and EA acknowledge support from the National Natural Science Foundation of China (NSFC) (Grants No. 12005049, No. 11935012). KM acknowledges support from Grant FJC2021-047840-I funded by MCIN/AEI/ 10.13039/501100011033 and by the European Union “NextGenerationEU/PRTR.” MHR acknowledges support from Ayuda PRE2021-098880 financiada por MCIN/AEI/ 10.13039/501100011033 y por el FSE+. MHR, AS, KM and MWM acknowledge the Spanish Ministry of Science MCIN with funding from NextGenerationEU (PRTR-C17.I1) and by Generalitat de Catalunya, “Severo Ochoa” Center of Excellence CEX2019-000910-S; projects SAPONARIA (PID2021-123813NB-I00) and MARICHAS (PID2021-126059OA-I00) funded by MCIN/ AEI /10.13039/501100011033/FEDER, EU; Generalitat de Catalunya through the CERCA program; Agència de Gestió d’Ajuts Universitaris i de Recerca Grant No. 2017-SGR-1354; Fundació Privada Cellex; Fundació Mir-Puig; The European Commission project OPMMEG (101099379).

-
- * KM and JK contributed equally to this work.
- [1] D. B. Orenes, R. J. Sewell, J. Lodewyck, and M. W. Mitchell, *Phys. Rev. Lett.* **128**, 153201 (2022).
 - [2] W. Bowden, A. Vianello, I. R. Hill, M. Schioppo, and R. Hobson, *Phys. Rev. X* **10**, 041052 (2020).
 - [3] D. Budker and M. Romalis, *Nature Physics* **3**, 227 (2007).
 - [4] C. Troullinou, R. Jiménez-Martínez, J. Kong, V. G. Lucivero, and M. W. Mitchell, *Phys. Rev. Lett.* **127**, 193601 (2021).
 - [5] M. W. Mitchell and S. Palacios Alvarez, *Rev. Mod. Phys.* **92**, 021001 (2020).
 - [6] S. Templier, P. Cheiney, Q. d’Armagnac de Castanet, B. Gouraud, H. Porte, F. Napolitano, P. Bouyer, B. Battelier, and B. Barrett, *Science Advances* **8**, eadd3854 (2022), <https://www.science.org/doi/pdf/10.1126/sciadv.add3854>.
 - [7] C. B. Møller, R. A. Thomas, G. Vasilakis, E. Zeuthen, Y. Tsaturyan, M. Balabas, K. Jensen, A. Schliesser, K. Hammerer, and E. S. Polzik, *Nature* **547**, 191 (2017).
 - [8] M. S. Safronova, D. Budker, D. DeMille, D. F. J. Kimball, A. Derevianko, and C. W. Clark, *Rev. Mod. Phys.* **90**, 025008 (2018).
 - [9] W. M. Itano, J. C. Bergquist, J. J. Bollinger, J. M. Gilligan, D. J. Heinzen, F. L. Moore, M. G. Raizen, and D. J. Wineland, *Phys. Rev. A* **47** (1993).
 - [10] K. Mouloudakis, G. Vasilakis, V. G. Lucivero, J. Kong, I. K. Kominis, and M. W. Mitchell, *Phys. Rev. A* **106**, 023112 (2022).
 - [11] S. Appelt, A. B.-A. Baranga, C. J. Erickson, M. V. Romalis, A. R. Young, and W. Happer, *Phys. Rev. A* **58**, 1412 (1998).
 - [12] O. Katz, R. Shaham, and O. Firstenberg, *PRX Quantum* **3**, 010305 (2022).
 - [13] J. L. Sørensen, J. Hald, and E. S. Polzik, *Phys. Rev. Lett.* **80** (1998).
 - [14] C. Gardiner, *Stochastic methods*, Vol. 4 (Springer Berlin, 2009).
 - [15] M. Koschorreck, M. Napolitano, B. Dubost, and M. W. Mitchell, *Physical Review Letters* **104**, 093602 (2010).
 - [16] G. Vasilakis, V. Shah, and M. V. Romalis, *Physical Review Letters* **106**, 143601 (2011).
 - [17] I. M. Savukov and M. V. Romalis, *Phys. Rev. A* **71**, 023405 (2005).
 - [18] E. Boto, S. S. Meyer, V. Shah, O. Alem, S. Knappe, P. Kruger, T. M. Fromhold, M. Lim, P. M. Glover, P. G. Morris, R. Bowtell, G. R. Barnes, and M. J. Brookes, *NeuroImage* **149**, 404 (2017).
 - [19] T. W. Kornack, R. K. Ghosh, and M. V. Romalis, *Physical Review Letters* **95**, 230801 (2005).
 - [20] J. Lee, A. Almasi, and M. Romalis, *Physical Review Letters* **120**, 161801 (2018).
 - [21] J. C. Allred, R. N. Lyman, T. W. Kornack, and M. V. Romalis, *Phys. Rev. Lett.* **89**, 130801 (2002).
 - [22] I. K. Kominis, T. W. Kornack, J. C. Allred, and M. V. Romalis, *Nature* **422** (2003).
 - [23] W. Happer and H. Tang, *Phys. Rev. Lett.* **31** (1973).
 - [24] W. Happer and A. C. Tam, *Phys. Rev. A* **16**, 1877 (1977).
 - [25] J. Kong, R. Jiménez-Martínez, C. Troullinou, V. G. Lucivero, G. Tóth, and M. W. Mitchell, *Nature Communications* **11** (2020), 10.1038/s41467-020-15899-1.
 - [26] K. Mouloudakis and I. K. Kominis, *Phys. Rev. A* **103**, L010401 (2021).
 - [27] E. Aleksandrov and V. Zapasskii, *Zh. Eksp. Teor. Fiz* **81** (1981).
 - [28] S. Crooker, D. Rickel, A. Balatsky, and D. Smith, *Nature* **431**, 49 (2004).
 - [29] G. E. Katsoprinakis, A. T. Dellis, and I. K. Kominis, *Phys. Rev. A* **75**, 042502 (2007).
 - [30] Y. Wen, X. Li, G. Zhang, and K. Zhao, *Phys. Rev. A* **104**, 063708 (2021).
 - [31] V. G. Lucivero, R. Jiménez-Martínez, J. Kong, and M. W. Mitchell, *Phys. Rev. A* **93**, 053802 (2016).
 - [32] S. Song, M. Jiang, Y. Qin, Y. Tong, W. Zhang, X. Qin, R.-B. Liu, and X. Peng, *Phys. Rev. Applied* **17**, L011001 (2022).
 - [33] M. Oestreich, M. Römer, R. J. Haug, and D. Hägele, *Phys. Rev. Lett.* **95**, 216603 (2005).
 - [34] V. G. Lucivero, N. D. McDonough, N. Dural, and M. V. Romalis, *Phys. Rev. A* **96**, 062702 (2017).
 - [35] V. Shah, G. Vasilakis, and M. V. Romalis, *Phys. Rev. Lett.* **104**, 013601 (2010).
 - [36] G. Vasilakis, H. Shen, K. Jensen, M. Balabas, D. Salart, B. Chen, and E. S. Polzik, *Nature Physics* **11** (2015).
 - [37] V. G. Lucivero, A. Dimic, J. Kong, R. Jiménez-Martínez, and M. W. Mitchell, *Phys. Rev. A* **95**, 041803 (2017).
 - [38] R. Jiménez-Martínez, J. Kołodyński, C. Troullinou, V. G. Lucivero, J. Kong, and M. W. Mitchell, *Physical Review Letters* **120**, 040503 (2018).
 - [39] W. Happer and B. S. Mathur, *Phys. Rev.* **163**, 12 (1967).
 - [40] T. Fernholz, H. Krauter, K. Jensen, J. F. Sherson, A. S. Sørensen, and E. S. Polzik, *Phys. Rev. Lett.* **101**, 073601 (2008).
 - [41] See Supplemental Online Material at [URL will be inserted by publisher] for more details.
 - [42] R. Shaham, O. Katz, and O. Firstenberg, *Phys. Rev. A* **102**, 012822 (2020).
 - [43] S. J. Seltzer, *Developments in alkali-metal atomic magnetometry* (Princeton University, 2008).

Supplementary Information for: *Anomalous spin projection noise in a spin-exchange-relaxation-free alkali-metal vapor*

K. Mouloudakis,^{1,*} J. Kong,^{2,*} A. Sierant,¹ E. Arkin,² M. Hernández Ruiz,¹ R. Jiménez-Martínez,³ and M. W. Mitchell^{1,4}

¹*ICFO - Institut de Ciències Fotòniques, The Barcelona Institute of Science and Technology, 08860 Castelldefels (Barcelona), Spain*

²*Department of Physics, Hangzhou Dianzi University, Hangzhou 310018, China*

³*FieldLine Industries, Boulder, Colorado 80303, USA*

⁴*ICREA-Institució Catalana de Recerca i Estudis Avançats, 08010 Barcelona, Spain*

CONTENTS

Magnetic field calibration	1
Frequency shifts	3
Coupled hyperfine Bloch equations	4
Observables	5
Spin-noise spectrum	6
Spin-noise power	7
RMS spectral averaging	8
References	9

MAGNETIC FIELD CALIBRATION

For calibrating the DC magnetic field experienced by the atoms, we perform spin-noise spectroscopy at $T \approx 100$ °C. By changing the current applied to the X-coil we follow the atomic response by monitoring the central frequency and the linewidth of the spin-noise resonance. The results are summarized in Fig.1. The precession frequency and the broadening are obtained by fitting the spectrum with a Lorentzian function $S(\nu) = S_0 + S_L \Gamma / [\Gamma^2 + (\nu - \nu_0)^2]$, in the vicinity of the resonance.

The flat response of the linewidth as a function of the applied current indicates safe operation away from the SERF regime as well as the absence of significant magnetic field gradients contributing to the spin-relaxation. The residual fields along the \hat{y} and \hat{z} directions have been obtained using the ground-state Hanle resonance (see caption of Fig.1) and compensated accordingly. The compensation measurement is performed at the temperature where the SERF spin-noise data were taken ($T \approx 169$ °C). We find a field of about 42 nT and 34 nT along the \hat{y} and \hat{z} directions, respectively.

At elevated temperature the vapor enters the SERF regime and both the precession frequency ω_q and the linewidth of the spin-noise resonance are altered. To experimentally obtain these two features we fit the power spectral density by a sum of a Lorentzian and a dispersive curve:

$$S(\nu) = S_0 + S_L \frac{\Gamma}{\Gamma^2 + (\nu - \nu_q)^2} + S_D \frac{\nu - \nu_q}{\Gamma^2 + (\nu - \nu_q)^2}. \quad (1)$$

where $\nu_q = \omega_q / 2\pi$. The fitting results for different magnetic fields are presented in the inset of Fig.2 of the main text. We find that the fitting model of Eq.(1) accurately captures the resonance features as illustrated with a representative example in Fig.2. Eq.(1) has been chosen in a phenomenological way, however it can be also justified by a more elaborate, first-principle theory for spin-noise in the SERF regime [2].

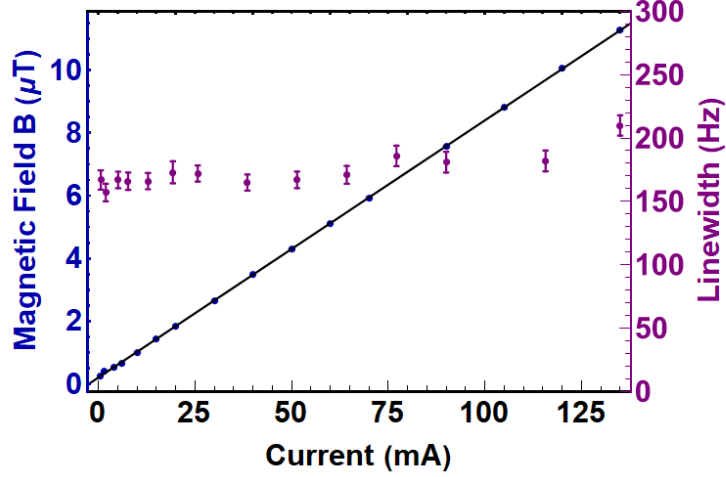


FIG. 1. **Magnetic-field calibration.** Extracted magnetic field and spin-noise linewidth (HWHM) as a function of the current applied to the coil along the \hat{x} -direction. The measurements are performed at a temperature of about $T \approx 100$ °C. The spin-noise resonances are fit with a Lorentzian function and the peak frequency is translated into magnetic field units using the ^{87}Rb gyromagnetic ratio $\gamma = g_s \mu_B / [2\pi\hbar(2I + 1)] = 6.998 \text{ Hz nT}^{-1}$. By fitting the magnetic field versus the applied current (black solid line) we obtain a field to current ratio of 82 nT mA^{-1} and a residual field of 202 nT along the \hat{x} -direction. The calibration equation reads $B(\mu\text{T}) = 0.202 + 0.082I$ where I has units of mA. At high temperature we have observed an additional DC field originating from the heater with a component along the \hat{x} -direction of 230 nT that is taken into account. The field components along the other two directions have been measured using the ground-state zero-field resonance of the atoms [1] and have been compensated by applying currents generated by a low-noise low-current source. The errors bars show the standard deviation of 150 fits on the different acquisitions during spectral averaging.

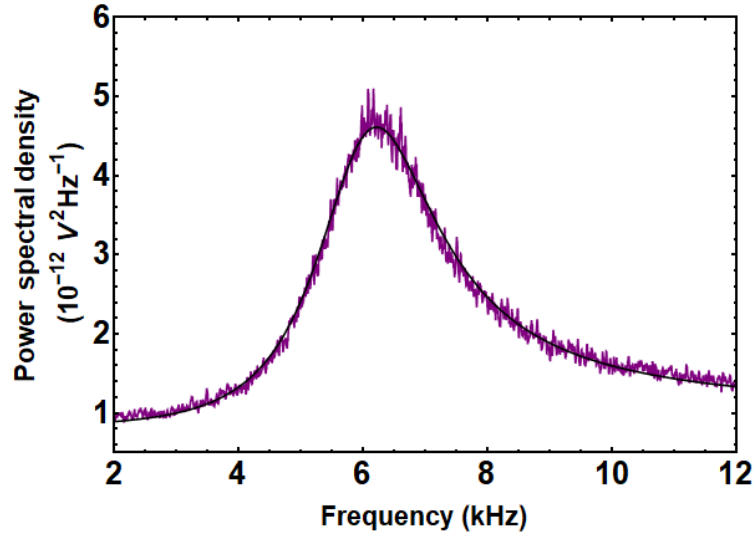


FIG. 2. **SPN peak frequency and linewidth:** A representative fit using Eq.(1) for finding the peak position and the linewidth of the spin-noise resonance. The fit yields $\nu_q = 5.99 \text{ kHz}$. For this particular example, the spectrum is fitted in the vicinity of the resonance in the frequency interval $\nu \in [2.0, 12.0] \text{ kHz}$ such that the resonance is clearly resolved. The corresponding magnetic field is $B \approx 1292 \text{ nT}$. We note that a simple Lorentzian model is inadequate to capture precisely the peak-position.

FREQUENCY SHIFTS

In the main text we use the shift of the spin-precession frequency of the spin-noise resonance to estimate the values of the different relaxation rates. Here we justify this reasoning by examining the various frequency shifts that spin-spin and atom-light interactions bring about on the ground-state energy levels of an unpolarized vapor, in the experimentally relevant case of high alkali-metal density and low magnetic fields. In the mean-field approximation, the evolution of the average spin density matrix of a single atom in the ground state is described by the density matrix equation [3, 4]

$$\begin{aligned} \frac{\partial \rho}{\partial t} = & -\frac{i}{\hbar} [A_{\text{hf}} \hat{\mathbf{I}} \cdot \hat{\mathbf{S}} + g_s \mu_B \hat{\mathbf{S}} \cdot \mathbf{B} + g_I \mu_N \hat{\mathbf{I}} \cdot \mathbf{B}, \rho] - \frac{i}{\hbar} [\delta\nu_{\text{ls}} + \delta\nu_{\text{se}} + \delta\nu_{\text{sd}}, \rho] \\ & + R_{\text{se}} [\phi(1 + 4\langle \hat{\mathbf{S}} \rangle \cdot \hat{\mathbf{S}}) - \rho] + R_L [\phi(1 + 2\mathbf{s} \cdot \hat{\mathbf{S}}) - \rho] + R_s(\phi - \rho) + D\nabla^2 \rho. \end{aligned} \quad (2)$$

The equation accounts for the change in the atomic spin state due to the different interactions that take place in the vapor cell. The most prominent are: i) hyperfine interaction between the electron and the nuclear spin, ii) Zeeman interactions of the electron and the nuclear spin with an externally applied magnetic field, iii) binary spin-exchange collisions between pairs of alkali-atoms that conserve the total electron spin of the interacting partners, iv) absorption of light leading to depolarization of the electron's spin, v) spin-rotation interaction which couples the alkali's electron spin to the rotational angular momentum of the colliding pair and vi) wall collisions during diffusion of the atoms into and out of the probe beam in the presence of buffer gas. The effects of magnetic field inhomogeneities on the state evolution are not considered here [5]. In addition, collisional interactions like SE or interactions that destroy electron's spin polarization (i.e., optical relaxation or $^{87}\text{Rb} - ^{87}\text{Rb}$ and $^{87}\text{Rb} - \text{N}_2$ spin-destruction collisions) cause linear frequency shifts accounted by the second commutator of Eq.(2). Here, $\delta\nu_{\text{ls}}$ is the optical light-shift due to the probe beam, $\delta\nu_{\text{se}}$ is the frequency shift due to spin-exchange collisions and $\delta\nu_{\text{sd}}$ is the frequency shift due to spin-destruction collisions. The derivation of the master equation and details about each particular interaction can be found in [6, 7]. To elucidate the following discussion on frequency shifts we briefly review each term of Eq.(2) and we define the various parameters showing up.

In the density matrix equation, A_{hf} is the coupling coefficient for the magnetic dipole interaction between the nuclear spin $\hat{\mathbf{I}}$ and the electron spin $\hat{\mathbf{S}}$, $g_s \approx 2.0$ is the electron g-factor, $\mu_B \approx 9.27 \times 10^{-24} \text{ J T}^{-1}$ is the Bohr magneton, $g_I \approx 5.5$ is the proton g-factor and $\mu_N \approx 5.05 \times 10^{-27} \text{ J T}^{-1}$ is the nuclear magneton. At low magnetic fields, the effect of the nuclear magnetic moment is to introduce a negligible frequency shift on the linear precession frequency of the atom by shifting the magnetic sublevels of the two hyperfine manifolds in opposite directions. We will neglect this shift since it is only a tiny fraction of ω_0 .

One way to describe the atom-light interaction is through a polarizability Hamiltonian that couples the light-polarization to the ground-state structure of the atom [8]. For far-detuned linearly polarized light ($\mathbf{s} = 0$), the mean light-shift $\delta\nu_{\text{ls}}$ is a consequence of the rank-1 vector polarizability operator and it is equal to zero. However, fluctuations in the right- and left- circular polarization can introduce light-shift (or backaction) noise, coupling to the spins as an effective fluctuating magnetic field with a white spectrum. It has been shown that light-shift noise has a negligible effect on unpolarized atoms [2]. More extensive discussions of the effects of light-shift back-action on unpolarized states can be found in [9–12]. The effect of the rank-2 tensor light-shift is related to the macroscopic feature of linear dichroism exhibited in the medium and is vanishing once the excited-state hyperfine manifolds cannot be resolved [13]. We note that in species different than alkali atoms, like for example in metastable helium, there are significant light-shifts observed through spin-noise spectroscopy [14].

For an unpolarized atom in equilibrium, the expectation value of the electron spin operator is $\langle \hat{\mathbf{S}} \rangle \approx 0$. Therefore, the SE frequency shift $\delta\nu_{\text{se}} = R_{\text{se}} \kappa_{\text{se}} \langle \hat{\mathbf{S}} \rangle \cdot \hat{\mathbf{S}}$, is considered negligible [15]. In contrast to spin-exchange collisions, the spin-rotation interaction is characterized by collisions of the electron spin with a large rotational angular momentum that can be approximated by a classical vector \mathbf{N} . The frequency shift due to the spin-rotation interaction is given by $\delta\nu_{\text{sd}} = \langle \boldsymbol{\varphi} \cdot \hat{\mathbf{S}} \rangle$ [16], where the angle $\boldsymbol{\varphi}$ is a vector of magnitude of the order of 10^{-4} radians, pointing along the direction of the classical angular momentum vector \mathbf{N} , $\boldsymbol{\varphi} \parallel \mathbf{N}$. The brackets $\langle \cdot \rangle$ denote an average over all possible collisional rotation angles. The rotation angle is equally likely to point in any direction, therefore we expect the frequency shift to be negligible. The term proportional to R_{se} describes the spin-exchange interaction, where $\phi = \sum_{i=0}^3 \hat{S}_i \rho \hat{S}_i$ is the electron-spin-depolarized density operator. Here, $\hat{S}_0 \equiv 1/2$ and $\{\hat{S}_1, \hat{S}_2, \hat{S}_3\} = \{\hat{S}_x, \hat{S}_y, \hat{S}_z\}$. Both the photon absorption from the probe beam and the spin-rotation interaction depolarize the electron spin of the atom in the ground state without affecting the nuclear spin state. Both these interactions can be combined into $R_{\text{sd}}(\phi - \rho)$ with $R_{\text{sd}} \equiv R_L + R_s$.

Finally, the effect of atomic diffusion on the spin-noise spectrum has been recently studied in [17, 18]. For a vapor

cell with buffer gas and a cell-diameter much larger than the diameter of a well-collimated Gaussian beam, the effect of diffusion is to depolarize the total atomic spin with a rate $R \propto D/(w(z)/2)^2$, where D is the diffusion constant of the alkali-metal atom and $w(z)$ is the beam waist. Therefore the atomic dynamics in the case of unpolarized atoms can be summarized by the following formula

$$\frac{d\rho}{dt} = -\frac{i}{\hbar}[A_{\text{hf}}\hat{\mathbf{I}} \cdot \hat{\mathbf{S}} + g_s\mu_B\hat{\mathbf{S}} \cdot \mathbf{B}, \rho] + R_{\text{se}}[\phi(1 + 4\langle\hat{\mathbf{S}} \cdot \hat{\mathbf{S}}\rangle - \rho) + R_{\text{sd}}(\phi - \rho) - R(\rho - \frac{1}{d}\mathbb{1})]. \quad (3)$$

Although the frequency shifts related to the spin-spin and atom-light interactions are negligible in the unpolarized state [19, 20], we emphasize that the opposite spin precession in the two ground-state manifolds in combination with the spin-exchange and spin-destruction collisions that transfer angular momentum between the two, can generate significant frequency shifts on the Zeeman sublevels [15, 21] that are quantified in the next section. The preceding shifts allow for precise determination of the spin-exchange rate as demonstrated in the main text and discussed in the following section.

COUPLED HYPERFINE BLOCH EQUATIONS

The paramagnetic Faraday rotation signal measured by the balanced photodetector is proportional to the collective angular momentum observables probed by the far-detuned and linearly polarized laser beam, and are defined as $\hat{\mathbf{F}}^\alpha \equiv \sum_{i=1}^{N_{\text{at}}} \hat{\mathbf{f}}_i^\alpha$, $\alpha \in \{a = I + 1/2, b = I - 1/2\}$, where $\hat{\mathbf{f}}_i^\alpha$ is the single-atom angular momentum observable of the i th atom, I is the nuclear spin and N_{at} is the total number of atoms contributing to the detected signal. In the case of an unpolarized atomic ensemble it has been shown [2, 15, 22, 23] that by expanding the density matrix equation of Eq.(3) in an irreducible, coupled spherical tensor operator basis, the collective angular momenta operators in the two hyperfine manifolds obey the following first order, coupled stochastic differential equations [24]

$$d\hat{\mathbf{F}}^a(t) = dt \left\{ \hat{\mathbf{F}}^a(t) \times \gamma_0 \mathbf{B} - R_{\text{se}} [\kappa_{aa}\hat{\mathbf{F}}^a(t) + \kappa_{ab}\hat{\mathbf{F}}^b(t)] - R_{\text{sd}} [\mu_{aa}\hat{\mathbf{F}}^a(t) + \mu_{ab}\hat{\mathbf{F}}^b(t)] - R\hat{\mathbf{F}}^a(t) \right\} + q_{aa}d\hat{\mathbf{W}}^a(t) + q_{ab}d\hat{\mathbf{W}}^b(t), \quad (4)$$

$$d\hat{\mathbf{F}}^b(t) = dt \left\{ -\hat{\mathbf{F}}^b(t) \times \gamma_0 \mathbf{B} - R_{\text{se}} [\kappa_{bb}\hat{\mathbf{F}}^b(t) + \kappa_{ba}\hat{\mathbf{F}}^a(t)] - R_{\text{sd}} [\mu_{bb}\hat{\mathbf{F}}^b(t) + \mu_{ba}\hat{\mathbf{F}}^a(t)] - R\hat{\mathbf{F}}^b(t) \right\} + q_{bb}d\hat{\mathbf{W}}^b(t) + q_{ba}d\hat{\mathbf{W}}^a(t). \quad (5)$$

Here $\gamma_0 = \gamma_e/(2I + 1)$ is the atomic gyromagnetic ratio with $\gamma_e = g_s\mu_B/\hbar \approx 2\pi \times 2.8 \times 10^4$ MHz T⁻¹ being the electron gyromagnetic ratio, when neglecting the small contribution of the nuclear Zeeman term, $\omega_0 = \gamma_0 B$ the linear Larmor frequency resulting from the diagonalization of the Breit-Rabi Hamiltonian $\hat{H} = A_{\text{hf}}\hat{\mathbf{I}} \cdot \hat{\mathbf{S}} + g_s\mu_B\hat{\mathbf{S}} \cdot \mathbf{B}$ at low magnetic fields (assuming the magnetic field has a component only along a single spatial direction) and $R_{\text{se}} = n\sigma_{\text{se}}\bar{u}$ is the spin-exchange rate with $\sigma_{\text{se}} \approx 2 \times 10^{-14}$ cm² being the spin-exchange cross-section and \bar{u} the relative thermal velocity of the pairwise collisions. The coefficients $\kappa_{\alpha\beta}$ and $\mu_{\alpha\beta}$ with $\alpha, \beta \in \{a, b\}$ describe the relaxation and the coupling between the two hyperfine multiplets due to spin-exchange and spin-destruction interactions, respectively. The spin-destructive interactions, like spin-destruction collisions between pairs of alkali atoms or between an alkali atom and an atom of the buffer gas, but also relaxation due to absorption from the probe beam are all captured by the rate $R_{\text{sd}} \equiv R_s + R_L$. For a ⁸⁷Rb vapor with $I = 3/2$, the coefficients entering Eqs.(4) and (5) are given by: $\kappa_{aa} = 1/8$, $\kappa_{ab} = -5/8$, $\kappa_{ba} = -1/8$, $\kappa_{bb} = 5/8$, $\mu_{aa} = 7/16$, $\mu_{ab} = -15/16$, $\mu_{ba} = -3/16$ and $\mu_{bb} = 11/16$. A detailed analysis of the origin of these coefficients can be found in [23]. Finally, we note that in this model we ignore effects of the detection backaction on the collective state of the vapor and relaxation caused by the coupling of the alkali spin to the vacuum polarization modes of the probe beam [25, 26].

Regarding the noise terms, $d\hat{\mathcal{W}}_j^\alpha(t)$ with $j \in \{x, y, z\}$ and $\alpha \in \{a, b\}$ represents white Gaussian noise with zero mean and variance dt and are associated with the spontaneous fluctuations of the collective angular momenta in the two hyperfine multiplets. The coefficients $q_{\alpha\beta}$ are the noise-strengths related to the interaction rates R_{se} , R_{sd} and R as a consequence of the fluctuation-dissipation theorem and are such to satisfy the equilibrium variance and covariance values given by $\text{Tr}[\rho_{\text{eq}}\hat{\mathbf{F}}_i^\alpha(0)\hat{\mathbf{F}}_j^\beta(0)]$, calculated at the many-body fully-mixed state, written as a product state $\rho_{\text{eq}} \equiv \rho_{\text{th}}^{\otimes N_{\text{at}}}$, where $\rho_{\text{th}} \equiv \mathbb{1}/d$ is the single-atom thermal state, and $d = (2a + 1) + (2b + 1)$ is the dimension of the single-atom space.

The system of differential equations of the two hyperfine angular momenta can be conveniently written in the compact form

$$d\hat{\mathbf{X}}(t) = A\hat{\mathbf{X}}(t)dt + Qd\hat{\mathbf{W}}(t), \quad (6)$$

where we define the angular momentum vector $\hat{\mathbf{X}}(t) \equiv [\hat{F}_x^a(t), \hat{F}_y^a(t), \hat{F}_z^a(t), \hat{F}_x^b(t), \hat{F}_y^b(t), \hat{F}_z^b(t)]^T$, the corresponding noise vector $d\hat{\mathbf{W}}(t) \equiv [d\hat{\mathcal{W}}_x^a(t), \dots, d\hat{\mathcal{W}}_z^b(t)]^T$, the 6×6 dynamics matrix A and the noise-strength matrix Q .

The real and imaginary parts of the eigenvalues of the dynamics matrix A correspond to the relaxation rate and the precession frequency of the magnetic resonance, respectively. In [15], analytical formulas for the eigenvalues as a function of $[I] = 2I + 1$ were presented, when only spin-exchange collisions were considered as a relaxation mechanism. Here, we derive generalized formulas for the eigenvalues taking into account spin-exchange, spin-destruction and spin-depolarizing collisions. In the high-density and low-field regime, the SE rate exceeds by far the other rates in the system. It is therefore apparent that R_{sd} is causing only small corrections in the frequency shift presented in [15].

$$\begin{aligned} \lambda = & -\left[R + \frac{[I]^2 + 2}{2[I]^2} R_{sd} + \frac{[I]^2 + 2}{3[I]^2} R_{se} \pm \sqrt{-\omega_0^2 + \left(\frac{[I]^2 - 2}{2[I]^2} R_{sd} + \frac{[I]^2 + 2}{3[I]^2} R_{se}\right)^2 - \frac{2[I]^2 - 8}{3[I]^4} R_{sd} R_{se} \pm \frac{i(R_{sd} + 2R_{se})\omega_0}{[I]}}\right] \\ \approx & -\left[R + \frac{[I]^2 + 2}{3[I]^2} R_{se} \pm \sqrt{-\omega_0^2 \pm \frac{2iR_{se}\omega_0}{[I]} + \left(\frac{[I]^2 + 2}{3[I]^2} R_{se}\right)^2}\right] - \mathcal{O}[R_{sd}]. \end{aligned} \quad (7)$$

To illustrate that indeed R_{sd} is contributing to only a small fraction in the frequency shift, in Fig.3 we plot the

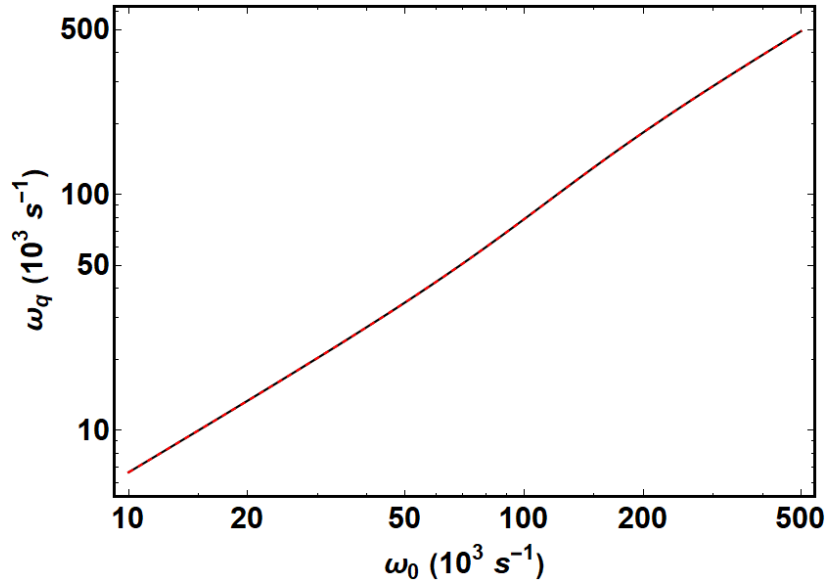


FIG. 3. **Frequency Shift:** Black solid line: Plot of $\text{Im}[\lambda]$ for $R_{se} = 3.02 \times 10^5 \text{ s}^{-1}$ and $R_{sd} = 0$. Red dashed line: same calculation with $R_{se} = 3.02 \times 10^5 \text{ s}^{-1}$ and $R_{sd} = 0.03 \times 10^5 \text{ s}^{-1}$.

$\omega_q = \text{Im}[\lambda]$ as a function of the Larmor frequency ω_0 for zero and non-zero value for R_{sd} . The red solid line shows the frequency shift only due to SE (zero-order in R_{sd}), whereas the black dashed line accounts also for the small correction due to spin-destruction. In calculating the transverse eigenvalues we assumed that the DC magnetic field is along the $\hat{\mathbf{x}}$ -direction, e.g., $\mathbf{B} = (B, 0, 0)$. We emphasize that spin-destruction behaves similarly to the spin-exchange collisions, since both interactions affect only the electronic part. As a consequence, in the dynamics for the angular momentum components there are effects similar to the SERF appearing, e.g., frequency shifts and slowing-down of the relaxation time. These effects were recently quantified in [21]. We note spin-depolarizing effects, like wall collisions (diffusion) do not cause any frequency shift, however they can have significant effect on the relaxation rate.

OBSERVABLES

In the small angle approximation [27], the quantum operator associated with the amplified differential photocurrent at the output of the balanced photodetector is proportional to the $\hat{S}_y(t)$ Stokes parameter, given by [28–30]

$$\hat{S}_y^{\text{out}}(t) \approx \hat{S}_y^{\text{in}}(t) + [g_a \hat{F}_z^a(t) - g_b \hat{F}_z^b(t)] \mathcal{S}_x^{\text{in}}(t), \quad (8)$$

where $\hat{\mathbf{F}}^\alpha(t) = (\hat{F}_x^\alpha(t), \hat{F}_y^\alpha(t), \hat{F}_z^\alpha(t))$, with $\alpha \in \{a, b\}$, are the two ground-state angular momentum vector operators. The dimensionless atom-light coupling coefficients g_α are defined as [12, 31]

$$g_\alpha \approx \frac{1}{2I+1} \frac{cr_e f_{\text{osc}}}{A_{\text{eff}}} \frac{\nu - \nu_\alpha}{(\nu - \nu_\alpha)^2 + (\frac{\Upsilon}{2})^2}, \quad (9)$$

where $r_e \approx 2.83 \times 10^{-15}$ m is the classical electron radius, $f_{\text{osc}} \approx 0.34$ is the oscillator strength associated with the D_1 transition of ^{87}Rb , $2I+1$ is the nuclear spin multiplicity, A_{eff} is the effective beam area as defined in the main text, Υ is the full width at half-maximum (FWHM) optical linewidth and $\nu - \nu_\alpha$ the optical detuning. The spin-noise power spectral density can be obtained once the following correlation function is calculated [2]

$$\begin{aligned} \mathcal{R}_{\hat{\mathcal{S}}_y^{\text{out}}, \hat{\mathcal{S}}_y^{\text{out}}}(\tau) &= \frac{1}{2} \langle \hat{\mathcal{S}}_y^{\text{out}}(\tau) \hat{\mathcal{S}}_y^{\text{out}}(0) + \hat{\mathcal{S}}_y^{\text{out}}(0) \hat{\mathcal{S}}_y^{\text{out}}(\tau) \rangle \\ &\approx \langle \Phi \rangle \delta(\tau) + \frac{\langle \Phi \rangle^2}{4} \left\{ g_a^2 \mathcal{R}_{\hat{F}_z^a, \hat{F}_z^a}(\tau) + g_b^2 \mathcal{R}_{\hat{F}_z^b, \hat{F}_z^b}(\tau) - g_a g_b [\mathcal{R}_{\hat{F}_z^a, \hat{F}_z^b}(\tau) + \mathcal{R}_{\hat{F}_z^b, \hat{F}_z^a}(\tau)] \right\}. \end{aligned} \quad (10)$$

with $\langle \Phi \rangle$ being the mean photon flux reaching the balanced polarimeter during a single acquisition run. The first term corresponds to photon shot noise while the second to the auto-correlation of the atomic-noise, separating the contribution of different hyperfine manifolds.

SPIN-NOISE SPECTRUM

In this section we summarize the main results presented in [2] and have been adapted in this work to describe and fit the experimental data. To describe the statistical properties of spin-noise it is necessary to use two-time correlation functions: for observables \hat{A} and \hat{B} , the covariance is $\mathcal{R}_{\hat{A}, \hat{B}}(\tau) \equiv \langle \hat{A}(\tau) \hat{B}(0) + \hat{B}(0) \hat{A}(\tau) \rangle / 2 = \text{Re}[\langle \hat{A}(\tau) \hat{B}(0) \rangle]$ since \hat{A} and \hat{B} are Hermitian operators and $(\hat{A}\hat{B})^\dagger = \hat{B}^\dagger \hat{A}^\dagger = \hat{B}\hat{A}$. Additionally, given a column vector of observables $\hat{\mathbf{V}}(t) = (\hat{A}, \hat{B}, \hat{C}, \dots)^T$ with stationary statistical properties, the covariance matrix is

$$\mathcal{R}_{\hat{\mathbf{V}}, \hat{\mathbf{V}}}(\tau) = \frac{1}{2} \left\{ \langle \hat{\mathbf{V}}(\tau) \hat{\mathbf{V}}^T(0) \rangle + [\langle \hat{\mathbf{V}}(0) \hat{\mathbf{V}}^T(\tau) \rangle]^T \right\} = \text{Re}[\langle \hat{\mathbf{V}}(\tau) \hat{\mathbf{V}}^T(0) \rangle] \quad (11)$$

where, $\langle \cdot \rangle$ denotes the average over different and independent realizations of the acquisition process. We assume the equilibrium many-body state as a fully-mixed state, which can be written as the product state $\rho_{\text{eq}} \equiv \rho_{\text{th}}^{\otimes N_{\text{at}}}$, where $\rho_{\text{th}} \equiv \mathbb{1}/d$ is the single-atom thermal state, and $d = (2a+1) + (2b+1)$ is the dimension of ρ . The steady state, equal-time correlators are given by the spin-projection noise, arising from the discreteness of the atomic observables

$$\mathcal{R}_{\hat{F}_i^\alpha, \hat{F}_j^\beta}(0) = \frac{1}{2} \langle \hat{F}_i^\alpha(0) \hat{F}_j^\beta(0) + \hat{F}_j^\beta(0) \hat{F}_i^\alpha(0) \rangle = \delta_{ij} \delta_{\alpha\beta} \frac{f^\alpha(f^\alpha+1)(2f^\alpha+1)}{6(2I+1)} N_{\text{at}} \equiv \delta_{ij} \delta_{\alpha\beta} \text{var}(F^\alpha), \quad (12)$$

where in the last step we defined $\text{var}(F^\alpha) \equiv f^\alpha(f^\alpha+1)(2f^\alpha+1)N_{\text{at}}/[6(2I+1)]$, being the variance of the angular momentum vector operator in the collective unpolarized state.

The drift matrix A and the noise-strength matrix Q are related to the equilibrium covariance matrix $\mathcal{R}_{\hat{\mathbf{x}}, \hat{\mathbf{x}}}(0)$ through the self-adjoint relationship [32]

$$A \mathcal{R}_{\hat{\mathbf{x}}, \hat{\mathbf{x}}}(0) + \mathcal{R}_{\hat{\mathbf{x}}, \hat{\mathbf{x}}}(0) A^T = Q Q^T. \quad (13)$$

In addition, the τ -dependence of the steady-state covariance matrix is given by

$$\mathcal{R}_{\hat{\mathbf{x}}, \hat{\mathbf{x}}}(\tau) = \begin{cases} e^{A\tau} \mathcal{R}_{\hat{\mathbf{x}}, \hat{\mathbf{x}}}(0) & , \tau > 0 \\ \mathcal{R}_{\hat{\mathbf{x}}, \hat{\mathbf{x}}}(0) e^{-A^T \tau} & , \tau < 0 \end{cases} \quad (14)$$

The power spectral density (assuming infinite acquisition time) is calculated as the Fourier transform of the branched unequal-time correlation function

$$S_{\hat{\mathbf{x}}, \hat{\mathbf{x}}}(\omega) = \int_{-\infty}^0 \mathcal{R}_{\hat{\mathbf{x}}, \hat{\mathbf{x}}}(0) e^{-A^T \tau} e^{-i\omega\tau} d\tau + \int_0^{+\infty} e^{A\tau} \mathcal{R}_{\hat{\mathbf{x}}, \hat{\mathbf{x}}}(0) e^{-i\omega\tau} d\tau. \quad (15)$$

We can express the power spectral density in terms of the eigenvalues of the matrix A by applying the spectral decomposition $e^{A\tau} = Ve^{\Lambda\tau}V^{-1}$ and by explicitly calculating the integral $\int_0^{+\infty} e^{[\Lambda - i\omega\mathbb{1}]\tau} d\tau = -(\Lambda - i\omega\mathbb{1})^{-1}$, yielding

$$S_{\hat{\mathbf{x}},\hat{\mathbf{x}}}(\omega) = -V(\Lambda - i\omega\mathbb{1})^{-1}V^{-1}\mathcal{R}_{\hat{\mathbf{x}},\hat{\mathbf{x}}}(0) + \text{c.c.} \quad (16)$$

Another useful and equivalent formula for the power spectral density is [32]

$$S_{\hat{\mathbf{x}},\hat{\mathbf{x}}}(\omega) = -\frac{1}{2\pi}(A + i\omega\mathbb{1})^{-1}QQ^T(A^T - i\omega\mathbb{1})^{-1} \quad (17)$$

where QQ^T is given by Eq.(13) since the equal-time covariance matrix is known. The preceding formula is preferable for fast numerical computations. Assuming that the probe beam is along the $\hat{\mathbf{z}}$ -direction, the total atomic power spectrum would be therefore

$$S_{\text{at}}(\omega) = \frac{r^2 G^2 P^2}{2\pi} \left\{ g_a^2 S_{\hat{F}_z^a, \hat{F}_z^a}(\omega) + g_b^2 S_{\hat{F}_z^b, \hat{F}_z^b}(\omega) - g_a g_b \left[S_{\hat{F}_z^a, \hat{F}_z^b}(\omega) + S_{\hat{F}_z^b, \hat{F}_z^a}(\omega) \right] \right\}. \quad (18)$$

Here G is the transimpedance gain of the PD, r the detector responsivity at 795 nm and P the mean laser power reaching the polarimeter during the acquisition. In Fig.1 of the main text, different spectral components of Eq.(18) are plotted as a function of frequency. Integration of the spectra of Eq.(18) in the frequency range of the experimentally relevant bandwidth yields the contribution of each spectral component on the total spin-noise power. Each spectrum is subsequently scaled by the off-resonant atom-light coupling coefficients $g_{a,b}$. The integration yields

$$\tilde{\mathcal{P}}_{\text{at}} = \mathcal{A} r^2 G^2 P^2 \left[g_a^2 \mathcal{P}_{\hat{F}_z^a, \hat{F}_z^a} + g_b^2 \mathcal{P}_{\hat{F}_z^b, \hat{F}_z^b} - g_a g_b \left(\mathcal{P}_{\hat{F}_z^a, \hat{F}_z^b} + \mathcal{P}_{\hat{F}_z^b, \hat{F}_z^a} \right) \right], \quad (19)$$

where $\tilde{\mathcal{P}}_{\text{at}} = \int_{\nu_{\text{low}}}^{\nu_{\text{high}}} S_{\text{at}}(\nu) d\nu$ with $\nu \in [\nu_{\text{low}}, \nu_{\text{high}}] \equiv [0.5 \text{ kHz}, \nu_{\text{bw}}]$. We limit the integration to 0.5 kHz in order to avoid low-frequency noise and to the maximum value of 95 kHz in order to avoid distortion in the noise power due to the anti-aliasing filter (The effect of the anti-aliasing filter of the acquisition system is taken into account in the theoretical calculation and has been simulated using a high-order low-pass filter as discussed in Section “RMS Spectral averaging” below).

Finally, we note that besides atomic noise, at low frequencies the excess technical noise can be significant. Sources of this type of noise are mostly thermal fluctuations in the optical fiber, imperfections in the extinction ratio of the Wollaston prism and air-density fluctuations during free-space propagation of the beam. Another source of low frequency noise is the noise spectrum of the longitudinal spin component, centered at $\nu = 0$, which can be observed when there is a non-zero field component along the beam direction.

SPIN-NOISE POWER

In the SERF regime, because of the non-Lorentzian character of the spectra, a significant portion of spin noise is spread over the high-frequency part of the spectrum. Since the acquisition is limited to 95 kHz, in Fig.4 we show what portion of the total noise is within this frequency range. This feature is illustrated in Fig. 4a) where $S_{\text{at}}(\nu)$ for $B = 385 \text{ nT}$ is numerically integrated up to different ν_{bw} and normalized as

$$\int_0^{\nu_{\text{bw}}} S_{\text{at}}(\nu) d\nu / \int_0^{\infty} S_{\text{at}}(\nu) d\nu, \quad (20)$$

where

$$\int_0^{\infty} S_{\text{at}}(\nu) d\nu = \frac{1}{2} \mathcal{A} r^2 G^2 P^2 [g_a^2 \text{var}(F^a) + g_b^2 \text{var}(F^b)], \quad (21)$$

is the total atomic noise in the signal for the particular experimental conditions.

Leveraging the agreement between theory and experiment, in Fig. 4b) we calculate the way the atomic noise of Fig. 4a) is distributed among different ground state hyperfine manifolds, for different measurement bandwidths. The noise within the different manifolds is expressed as a percentage of the total noise as obtained in Fig. 4a). The calculation is based on Eq.(19). It is apparent that the noise in the upper hyperfine manifold can be 120% of the total noise, however strong noise coupling between the two hyperfine levels (up to 40% of the total noise) is subtracted from the noise in the upper and lower manifolds (see Eq.(19)) to obtain the final amount, being the one that is

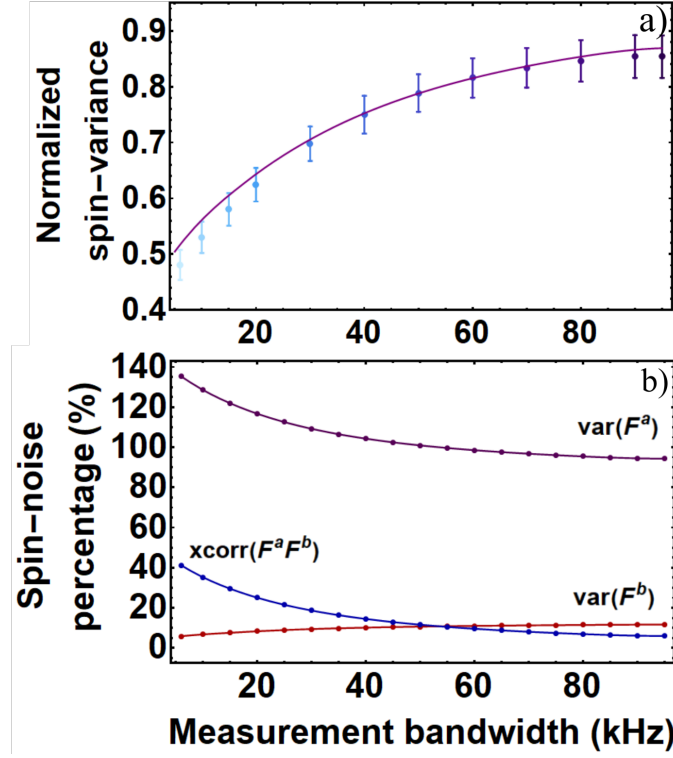


FIG. 4. **a)** Integrated spin-noise spectrum up to different effective measurement bandwidths ν_{bw} for a fixed magnetic field of $B = 385$ nT. The noise is normalized to $g_a^2 \text{var}(F^a) + g_b^2 \text{var}(F^b)$ (see text). Purple solid line is the prediction of the theory. **b)** The plot shows theoretical prediction on how the noise obtained in graph **a)** is distributed at different hyperfine levels, for different measurement bandwidths (see text). Solid lines are interpolations of theoretical predictions indicated by single points in the graph. Purple, red and blue solid lines indicate the noise contribution of the upper, the lower and the cross hyperfine spectra, respectively.

experimentally accessible. We point out that these percentages depend strongly on the detuning, a different choice of which can alter the balance of the noises coupled in the signal [2].

In Fig. 5a), the transition from the slow SE ($R_{se} \ll \omega_0$) to the rapid SE regime ($R_{se} \gg \omega_0$) is demonstrated for a fixed magnetic field of $B = 918$ nT, while the ^{87}Rb number density is altered. The spin-noise power for different cut-off frequencies (effective measurement bandwidths) as the number density is altered, is shown in Fig. 5b). In contrast to the slow SE regime where the noise is constant and concentrated in the vicinity of the resonance frequency, there is significant redistribution of noise when the vapor enters the SERF regime that can be controlled as the measurement bandwidth is limited. Finally, in the inset of Fig. 5b) we show that for different cut-off frequencies the SERF dynamics result in spin-noise power that scales differently with the number density.

RMS SPECTRAL AVERAGING

The spin-noise spectra have been obtained by performing discrete Fourier transform to the acquired time traces $X(j)$ where j is the j th sample. Assuming a total number of samples N , we define the FFT as

$$Y(k) = \frac{1}{N} \sum_{j=1}^N X(j) e^{-2\pi i(j-1)(k-1)/N}. \quad (22)$$

Given N_{rep} subsequent acquisitions, the RMS averaging of the complex FFT spectra are obtained as

$$Y_{\text{rms}}^R(k) = \sqrt{\frac{1}{N_{\text{rep}}} \sum_{i=1}^{N_{\text{rep}}} \text{Re}[Y_i(k)]^2}, \quad (23)$$

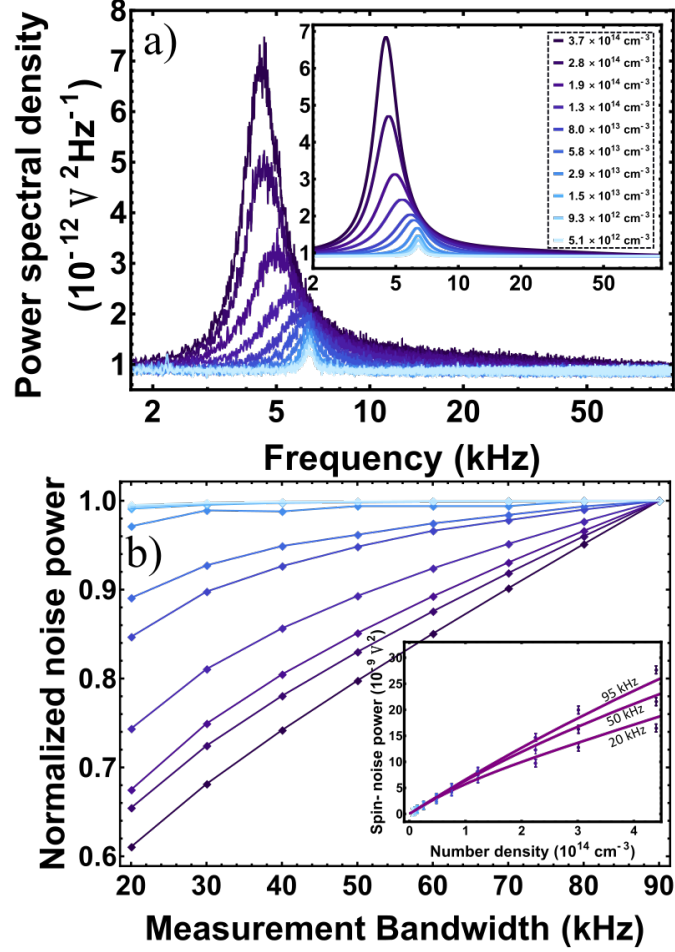


FIG. 5. **a)** Transition to the SERF regime for a fixed magnetic field of $B = 918$ nT and increasing number density (see legend in the inset), as shown in the inset using the first principles theory. Far wings imitating PSN are apparent in the spectra. **b)** Spin-noise power as a function of the measurement bandwidth for different number densities, for the spectra presented in **a)**. The noise is normalized to the noise in the bandwidth of 95 kHz. Inset shows the scaling of the integrated spin-noise power with the ^{87}Rb number density for three different effective measurement bandwidths (20, 50 and 95 kHz). Purple solid lines indicate the theoretical expectation.

$$Y_{\text{rms}}^I(k) = \sqrt{\frac{1}{N_{\text{rep}}} \sum_{i=1}^{N_{\text{rep}}} \text{Im}[Y_i(k)]^2}, \quad (24)$$

where $Y_i(k)$ is the FFT spectrum of the i th repetition of the acquisition run and $Y_{\text{rms}}(k) \equiv Y_{\text{rms}}^R(k) + iY_{\text{rms}}^I(k)$. The power spectral density is therefore

$$S_{\text{rms}}(k) = \frac{1}{\delta f n_w} \left(\text{Re}[Y_{\text{rms}}(k)]^2 + \text{Im}[Y_{\text{rms}}(k)]^2 \right), \quad (25)$$

where $\delta f = 1/T_{\text{acq}}$ is the frequency bin, T_{acq} the total acquisition time and n_w is the noise per window bandwidth. We use a uniform window with $n_w = 1$. We observe that a Hanning window of the form $w(j) = 1 - \cos(2\pi(j-1)/N)$ is not altering the results presented herein. As mentioned in the main text, in the calculation of spin-noise power, a low-pass filter is applied to simulate the anti-aliasing filter of the DAQ system (see Fig.6).

-
- [1] C. Cohen-Tannoudji, J. Dupont-Roc, S. Haroche, and F. Laloë, *Revue de Physique Appliquée* **5**, 102 (1970).
 - [2] K. Mouloudakis, G. Vasilakis, V. G. Lucivero, J. Kong,

* KM and JK contributed equally to this work.

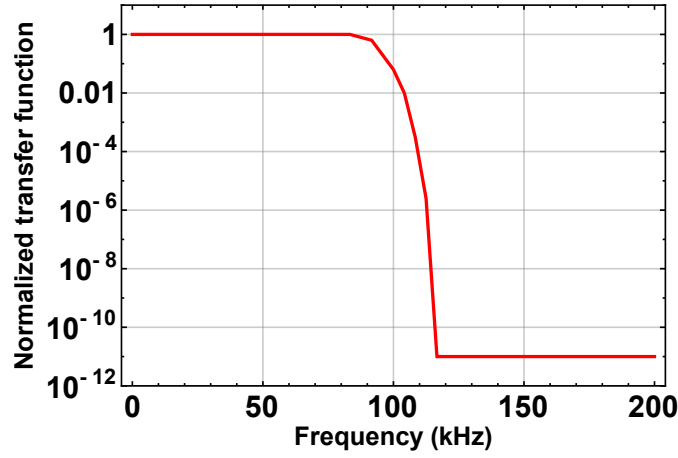


FIG. 6. **Anti-aliasing, low-pass filter:** To precisely capture the behavior of the anti-aliasing filter applied by the DAQ system on the spin-noise power we simulate the filter using an interpolated function as shown above. The transfer function of the interpolated filter presents a steep roll-off at the cut-off frequency of 96.8 kHz.

- I. K. Kominis, and M. W. Mitchell, Phys. Rev. A **106**, 023112 (2022).
- [3] S. Appelt, A. B.-A. Baranga, C. J. Erickson, M. V. Romalis, A. R. Young, and W. Happer, Phys. Rev. A **58**, 1412 (1998).
- [4] O. Katz and O. Firstenberg, Phys. Rev. A **98**, 012712 (2018).
- [5] G. D. Cates, S. R. Schaefer, and W. Happer, Phys. Rev. A **37** (1988).
- [6] W. Happer, Y. Y. Jau, and T. Walker, *Optically Pumped Atoms* (Wiley, 2010).
- [7] W. Happer, Rev. Mod. Phys. **44**, 169 (1972).
- [8] W. Happer and B. S. Mathur, Phys. Rev. **163**, 12 (1967).
- [9] G. Tóth and M. W. Mitchell, New Journal of Physics **12**, 053007 (2010).
- [10] N. Behbood, G. Colangelo, F. Martin Ciurana, M. Napolitano, R. J. Sewell, and M. W. Mitchell, Physical Review Letters **111**, 103601 (2013).
- [11] N. Behbood, F. Martin Ciurana, G. Colangelo, M. Napolitano, G. Tóth, R. J. Sewell, and M. W. Mitchell, Physical Review Letters **113**, 093601 (2014).
- [12] J. Kong, R. Jiménez-Martínez, C. Troullinou, V. G. Lucivero, G. Tóth, and M. W. Mitchell, Nature Communications **11** (2020), 10.1038/s41467-020-15899-1.
- [13] W. Happer, Progress in Quantum Electronics **1** (1970).
- [14] J. Delpy, S. Liu, P. Neveu, E. Wu, F. Bretenaker, and F. Goldfarb, arXiv preprint arXiv:2212.00401 (2022).
- [15] W. Happer and A. C. Tam, Phys. Rev. A **16**, 1877 (1977).
- [16] W. Happer and W. Van Wijngaarden, Hyperfine Interact (1987) 38: 435 **38**, 435 (1987).
- [17] V. G. Lucivero, N. D. McDonough, N. Dural, and M. V. Romalis, Phys. Rev. A **96**, 062702 (2017).
- [18] R. Shagam, O. Katz, and O. Firstenberg, Phys. Rev. A **102**, 012822 (2020).
- [19] K. Mouloudakis and I. K. Kominis, Phys. Rev. A **103**, L010401 (2021).
- [20] K. Mouloudakis, M. Loulakis, and I. K. Kominis, Phys. Rev. Res. **1**, 033017 (2019).
- [21] M. Dikopoltsev, A. Berrebi, U. Levy, and O. Katz, arXiv preprint arXiv:2209.12236 (2022).
- [22] O. Katz, O. Peleg, and O. Firstenberg, Phys. Rev. Lett. **115**, 113003 (2015).
- [23] W. Xiao, T. Wu, X. Peng, and H. Guo, Phys. Rev. A **103**, 043116 (2021).
- [24] Note this is the case only for unpolarized or low-polarized ensembles under certain assumptions. The validity of these equations has been described in [2].
- [25] J. K. Stockton, R. van Handel, and H. Mabuchi, Phys. Rev. A **70**, 022106 (2004).
- [26] R. L. Cook, C. A. Riofrío, and I. H. Deutsch, Phys. Rev. A **90**, 032113 (2014).
- [27] B. Julsgaard, A. Kozhekin, and E. S. Polzik, Nature **413**, 400 (2001).
- [28] K. Hammerer, A. S. Sørensen, and E. S. Polzik, Rev. Mod. Phys. **82** (2010).
- [29] G. Colangelo, C. F. Martin, B. L. C., S. R. J., and M. M. W., Nature **543**, 525 (2017).
- [30] G. Colangelo, R. J. Sewell, N. Behbood, F. M. Ciurana, G. Triginer, and M. W. Mitchell, New Journal of Physics **15**, 103007 (2013).
- [31] R. Jiménez-Martínez, J. Kołodyński, C. Troullinou, V. G. Lucivero, J. Kong, and M. W. Mitchell, Physical Review Letters **120**, 040503 (2018).
- [32] C. Gardiner, *Stochastic methods*, Vol. 4 (Springer Berlin, 2009).